Center for Turbulence Research
Annual Research Briefs 2018

The most effective interface disturbance of a round liquid jet

By H. Hwang AND M. J. P. Hack

1. Motivation and objectives

Primary atomization of liquid jets injected into a gas environment originates from the distortion and eventual disintegration of the interface between the two phases. The resulting formation of liquid droplets is of fundamental relevance to various applications such as medical inhalers and internal combustion engines.

The atomization process of liquid jets is often understood as a sequence of instability events, as proposed, for instance, by Marmottant & Villermaux (2004). Past the exit of the nozzle, the velocity difference between the liquid and the surrounding gas promotes an inviscid shear-layer Kelvin-Helmholtz instability that induces a primary distortion of the jet interface. Depending on the flow parameters, this distortion is either axisymmetric or helical (see, e.g., Hoyt & Taylor 1977; Chigier 1989). Together with the difference in density between the gas and liquid phases, the primary distortion can make the flow susceptible to secondary Rayleigh-Taylor instabilities. The Rayleigh-Taylor instability gives rise to ligaments that are distributed around the circumference of the jet. If the ligaments are sufficiently stretched, capillary effects in the form of a Plateau-Rayleigh instability can cause their pinch off and their eventual breakup into a number of small droplets. Depending on the flow parameters, the jet as a whole may alternatively also break up into segments via Plateau-Rayleigh instability, as discussed, for instance, by Lasheras & Hopfinger (2000).

Linear stability theory has been the method of choice for a number of researchers who sought to predict the length scales during the early stages of jet atomization (see, e.g., Bague *et al.* 2010). The analysis has been oftentimes simplified by representing the curved interface of the jet through planar shear flow (see, e.g., Yecko *et al.* 2002; Bague *et al.* 2010). This approach can be justified in settings where the thickness of the shear layer on the liquid side of the interface is appreciably smaller than the jet radius, but it breaks down, for instance, when the flow exiting the nozzle approaches developed pipe flow. Preziosi *et al.* (1989) and Lin & Ibrahim (1990) conducted linearized stability analyses of symmetric arrangements of two liquids in core-annular Poiseuille flow through round pipes by using a Galerkin projection with two orthogonal sets of functions and a pseudospectral method. Their results indicated a linearly stable regime for a range of Reynolds numbers, which at its lower end is limited by the emergence of a capillary Plateau-Rayleigh instability. On the other hand, sufficiently high Reynolds numbers trigger a shear-driven Kelvin-Helmholtz instability.

Even when the eigenvalue spectrum reveals a flow as exponentially stable, the non-normal nature of the eigenfunctions of the linearized governing equations can allow a transient energy gain of the linear system that is ultimately overcome by viscous decay. The analysis of this transient amplification of disturbances can be cast into an optimization problem in terms of the perturbation kinetic energy (Reddy & Henningson 1993). Boronin *et al.* (2013) applied a similar approach to a two-phase round viscous fluid jet.

However, their study focused on optimizing the kinetic energy of perturbations, which in itself is not particularly meaningful in the context of primary atomization. Foures *et al.* (2012) present a variational framework for constrained optimization of spatially and temporally evolving flows. The approach allows a partitioning of the state vector and thus the optimization of individual components of the full state.

In this study, we explore the most effective interface distortions, which during a given time interval maximize the surface tension energy of the interface of a round liquid jet. We focus particularly on flow configurations that are exponentially stable and as such preclude the distortion of the jet interface by classical instability mechanisms such as Kelvin-Helmholtz and Plateau-Rayleigh. The objective of identifying the most effective disturbances is cast as an optimization problem that is solved by means of singular value decomposition. A cylindrical formulation of the governing equations is discretized using a Chebyshev spectral collocation method. The analysis incorporates both gas and liquid viscosity as well as surface tension. The base flow for the linear stability analysis is computed from numerical simulations. Energy budget terms are derived for the general case of a nonaxisymmetric jet and evaluated to analyze the underlying physical mechanisms.

2. Methodology

2.1. *Nondimensional parameters*

The radius, R, and the local centerline velocity, U_c, of the jet are chosen as the characteristic length and characteristic velocity throughout this work. The Weber number and the Reynolds number are defined based on the parameters of the liquid phase. Including the viscosity ratio, m, and the density ratio, η, the four independent parameters of the system are thus

$$m = \frac{\mu_g}{\mu_l}, \qquad \eta = \frac{\rho_g}{\rho_l}, \qquad Re_l = \frac{\rho_l U_c R}{\mu_l}, \qquad We = \frac{\rho_l U_c^2 R}{\sigma}. \tag{2.1}$$

2.2. *Linear analysis*

Within this study, we consider the behavior of infinitesimal disturbances to an incompressible steady base flow representing a round jet injected into a stationary environment. The analysis is based on the governing equations in cylindrical coordinates, where z, r and θ denote the axial, radial and azimuthal dimensions, respectively. The axial expansion of the jet is assumed to be small and as such is disregarded in the following, leading to a base flow of the form $\boldsymbol{U} = \left[U\left(r\right), 0, 0\right]^T$. Linearization of the Navier-Stokes equations for each fluid phase leads to

$$\frac{\partial u}{\partial t} + U\frac{\partial u}{\partial z} = -\frac{\partial p}{\partial z} + \frac{1}{Re}\nabla^2 u, \tag{2.2}$$

$$\frac{\partial v}{\partial t} + U\frac{\partial v}{\partial z} + vU' = -\frac{\partial p}{\partial r} + \frac{1}{Re}\left(\nabla^2 v - \frac{v}{r^2} - \frac{2}{r^2}\frac{\partial w}{\partial \theta}\right), \tag{2.3}$$

$$\frac{\partial w}{\partial t} + U\frac{\partial w}{\partial z} = -\frac{1}{r}\frac{\partial p}{\partial \theta} + \frac{1}{Re}\left(\nabla^2 w + \frac{2}{r^2}\frac{\partial v}{\partial \theta} - \frac{w}{r^2}\right), \tag{2.4}$$

$$\frac{\partial u}{\partial z} + \frac{1}{r}\frac{\partial}{\partial r}(rv) + \frac{\partial w}{\partial \theta} = 0, \tag{2.5}$$

where u, v and w are the velocity disturbances in the axial, radial and azimuthal directions, respectively, and U' denotes the derivative of the base flow in the radial dimension.

Homogeneity of the base flow in the x, θ and t dimensions allows a normal–mode ansatz for the disturbances, which are assumed to have the form

$$[u, v, w, p] = [\widehat{u}(r), \mathrm{i}\widehat{v}(r), \widehat{w}(r), \widehat{p}(r)]\, \mathrm{e}^{\mathrm{i}(\alpha z + n\theta - \omega t)}, \tag{2.6}$$

where α and n denote the streamwise and discrete azimuthal wavenumber, respectively, and ω represents the frequency of the disturbance. Note that in the radial dimension, the ansatz is multiplied by the imaginary unit i to match the phase of the disturbance with the other components in the continuity equation, Eq. (2.5) (see, e.g., Khorrami *et al.* 1989). Substitution of the ansatz, Eq. (2.6), into the the governing equations, Eqs. (2.2)–(2.5), results in the following set of equations

$$\left\{-\frac{1}{Re}\frac{\mathrm{d}^2}{\mathrm{d}y^2} - \frac{1}{Re}\frac{1}{r}\frac{\mathrm{d}}{\mathrm{d}y} + \left[-\mathrm{i}\omega + \mathrm{i}\alpha U + \frac{1}{Re}\left(\frac{n^2+1}{r^2} + \alpha^2\right)\right]\right\}\widehat{u} + \frac{1}{Re}\frac{2n}{r^2}\widehat{v} + \frac{\mathrm{i}n}{r}\widehat{p} = 0, \tag{2.7}$$

$$\left\{-\frac{\mathrm{i}}{Re}\frac{\mathrm{d}^2}{\mathrm{d}y^2} - \frac{\mathrm{i}}{Re}\frac{1}{r}\frac{\mathrm{d}}{\mathrm{d}y} + \left[\omega - \alpha U + \frac{\mathrm{i}}{Re}\left(\frac{n^2+1}{r^2} + \alpha^2\right)\right]\right\}\widehat{v} + \frac{1}{Re}\frac{\mathrm{i}2n}{r^2}\widehat{u} + \frac{\mathrm{d}\widehat{p}}{\mathrm{d}y} = 0, \tag{2.8}$$

$$\left\{-\frac{1}{Re}\frac{\mathrm{d}^2}{\mathrm{d}y^2} - \frac{1}{Re}\frac{1}{r}\frac{\mathrm{d}}{\mathrm{d}y} + \left[-\mathrm{i}\omega + \mathrm{i}\alpha U + \frac{1}{Re}\left(\frac{n^2}{r^2} + \alpha^2\right)\right]\right\}\widehat{w} + \mathrm{i}U'\frac{\mathrm{d}\widehat{v}}{\mathrm{d}y} + \mathrm{i}\alpha\widehat{p} = 0, \tag{2.9}$$

$$\frac{n}{r}\widehat{u} + \left(\frac{\mathrm{d}}{\mathrm{d}y} + \frac{1}{r}\right)\widehat{v} + \alpha\widehat{w} = 0. \tag{2.10}$$

The disturbance of the interface between the two phases is represented by the complex interface displacement, $\widehat{f}$. The interface disturbance is assumed to be small and satisfies the following kinematic condition

$$\frac{\mathrm{d}f}{\mathrm{d}t} = \left(\frac{\partial}{\partial t} + U\frac{\partial}{\partial z}\right)\widehat{f} = \left(-\mathrm{i}\omega + \mathrm{i}\alpha U_l^I\right)\widehat{f} = v_l^I. \tag{2.11}$$

Here, the superscript I denotes quantities evaluated at the interface. The full disturbance state vector thus becomes

$$\widehat{\boldsymbol{q}} = \begin{bmatrix}\widehat{u}_g(y) & \widehat{v}_g(y) & \widehat{w}_g(y) & \widehat{p}_g(y) & \widehat{f} & \widehat{u}_l(y) & \widehat{v}_l(y) & \widehat{w}_l(y) & \widehat{p}_l(y)\end{bmatrix}^T. \tag{2.12}$$

We arrive at the temporal stability eigenvalue problem by prescribing a real streamwise wavenumber α and an integer azimuthal wavenumber n and by assuming a complex frequency ω. Since only certain ω solve the resulting equations, we arrive at an eigenvalue problem that can be written as

$$\mathrm{i}\omega\mathsf{M}\widehat{\boldsymbol{q}} = \mathsf{L}\widehat{\boldsymbol{q}} \tag{2.13}$$

with

$$\mathsf{M} = \begin{pmatrix}\widetilde{\mathsf{M}} & 0 & 0\\ 0 & -1 & 0\\ 0 & 0 & \widetilde{\mathsf{M}}\end{pmatrix} \tag{2.14}$$

and

$$\mathsf{L} = \begin{pmatrix}\mathsf{L}_j & 0 & 0\\ 0 & -\mathrm{i}\alpha U^I & \widetilde{\mathsf{L}}\\ 0 & 0 & \mathsf{L}_j\end{pmatrix}. \tag{2.15}$$

The block matrices $\widetilde{\mathsf{M}}$, $\widetilde{\mathsf{L}}$ and L_j are defined as

$$\widetilde{\mathsf{M}} = \begin{pmatrix} 0 & 0 & 1 & 0 \\ \mathrm{i} & 0 & 0 & 0 \\ 0 & 1 & 0 & 0 \\ 0 & 0 & 0 & 0 \end{pmatrix}, \tag{2.16}$$

$$\mathsf{L}_j = \begin{pmatrix} \mathrm{i}U' & 0 & \mathcal{U}_j & \mathrm{i}\alpha \\ \mathcal{V}_j & \mathrm{i}\frac{1}{Re_j}\frac{2n}{r^2} & 0 & \frac{\mathrm{d}}{\mathrm{d}y} \\ \frac{1}{Re_j}\frac{2n}{r^2} & \mathcal{W}_j & 0 & \mathrm{i}\frac{n}{r} \\ \mathcal{P}_j & \frac{n}{r} & \alpha & 0 \end{pmatrix}, \tag{2.17}$$

$$\widetilde{\mathsf{L}} = [0 \quad \mathrm{i} \quad 0 \quad 0]\,. \tag{2.18}$$

The elements of the matrices L_j are

$$\mathcal{U}_j = -\frac{1}{Re_j}\frac{\mathrm{d}^2}{\mathrm{d}y^2} - \frac{1}{Re_j}\frac{1}{r}\frac{\mathrm{d}}{\mathrm{d}y} + \left\{\mathrm{i}\alpha U + \frac{1}{Re_j}\left(\frac{n^2}{r^2} + \alpha^2\right)\right\}, \tag{2.19}$$

$$\mathcal{V}_j = -\frac{\mathrm{i}}{Re_j}\frac{\mathrm{d}^2}{\mathrm{d}y^2} - \frac{\mathrm{i}}{Re_j}\frac{1}{r}\frac{\mathrm{d}}{\mathrm{d}y} + \left\{-\alpha U + \frac{\mathrm{i}}{Re_j}\left(\frac{n^2+1}{r^2} + \alpha^2\right)\right\}, \tag{2.20}$$

$$\mathcal{W}_j = -\frac{1}{Re_j}\frac{\mathrm{d}^2}{\mathrm{d}y^2} - \frac{1}{Re_j}\frac{1}{r}\frac{\mathrm{d}}{\mathrm{d}y} + \left\{\mathrm{i}\alpha U + \frac{1}{Re_j}\left(\frac{n^2+1}{r^2} + \alpha^2\right)\right\}, \tag{2.21}$$

$$\mathcal{P}_j = \frac{\mathrm{d}}{\mathrm{d}y} + \frac{1}{r}, \tag{2.22}$$

where the subscript j indicates either gas (g) or liquid (l) phase. Note that the Reynolds numbers in Eqs. (2.19)–(2.21) are related through

$$Re_g = \frac{\eta}{m} Re_l. \tag{2.23}$$

2.3. *Boundary conditions and interface conditions*

No–slip and no–penetration boundary conditions are imposed on the eigenfunctions in the far field of the gas phase. Therefore, the boundary conditions at the top of the gas phase domain become

$$\widehat{v}_g = 0, \qquad \mathcal{D}\widehat{v}_g = 0, \qquad \widehat{\eta}_g = 0, \qquad \text{at} \quad y = L_g. \tag{2.24}$$

Special care has to be taken at the centerline because of the singular nature of the co-ordinate system. All physical quantities are assumed to be smooth and bounded at the centerline, leading to the following treatment as $r \to 0$ (Khorrami *et al.* 1989)

$$\lim_{r\to 0} \frac{\partial \widehat{\mathbf{u}}}{\partial \theta} = \frac{\partial}{\partial \theta}\left(\widehat{u}\mathbf{e}_z + \widehat{v}\mathbf{e}_r + \widehat{w}\mathbf{e}_\theta\right) = 0 \tag{2.25}$$

and

$$\lim_{r\to 0} \frac{\partial \widehat{p}}{\partial \theta} = 0. \tag{2.26}$$

Substitution of the normal–mode assumption, Eq. (2.6), for the disturbances into Eqs. (2.25)–(2.26) yields the following expressions

$$n\widehat{v} + \widehat{w} = 0, \quad \widehat{v} + n\widehat{w} = 0, \quad n\widehat{u} = 0, \quad n\widehat{p} = 0. \tag{2.27}$$

The resulting centerline conditions depend on the discrete azimuthal number, n, as follows

$$\frac{\mathrm{d}\widehat{u}}{\mathrm{d}y}=0, \qquad \widehat{v}=0, \qquad \widehat{w}=0, \qquad \frac{\mathrm{d}\widehat{p}}{\mathrm{d}y}=0, \qquad \text{if} \quad n=0, \tag{2.28}$$

$$\widehat{u}=0, \qquad \mathrm{i}\widehat{v}-\widehat{w}=0, \qquad 2\frac{\mathrm{d}\widehat{v}}{\mathrm{d}y}+\mathrm{i}\frac{\mathrm{d}\widehat{w}}{\mathrm{d}y}=0, \qquad \widehat{p}=0, \qquad \text{if} \quad n=-1 \text{ or } 1, \tag{2.29}$$

$$\widehat{u}=0, \qquad \widehat{v}=0, \qquad \widehat{w}=0, \qquad \widehat{p}=0, \qquad \text{otherwise.} \tag{2.30}$$

Across the interface, velocities and tangential stresses are continuous while the normal stress jumps proportional to the surface tension, leading to the following set of interface conditions

$$\mathcal{J}(\widehat{u})=-\mathcal{J}\left(\frac{\mathrm{d}U}{\mathrm{d}r}\right)\widehat{f}, \qquad \mathcal{J}(\widehat{v})=0, \qquad \mathcal{J}(\widehat{w})=0, \tag{2.31}$$

$$\mathcal{J}(\widehat{\tau}_{zr})=-\mathcal{J}\left(\mu\frac{\mathrm{d}^2U}{\mathrm{d}r^2}\right)\widehat{f}, \qquad \mathcal{J}(\widehat{\tau}_{\theta r})=0, \qquad \mathcal{J}(\widehat{\tau}_{rr})=\sigma\nabla^2\widehat{f}. \tag{2.32}$$

Here, $\mathcal{J}(\mathcal{X})$ is the difference in $\mathcal{X}$ between the two phases at the interface, for instance, $\mathcal{J}(u)=u_g-u_l$. Note that the jump conditions for $\widehat{u}$ and $\widehat{\tau}_{zr}$ have been derived by employing a first–order Taylor expansion, implying that $U_j(r=1+f)=U_j^I+(\mathrm{d}U_j^I/\mathrm{d}r)\widehat{f}$. In terms of the components of the disturbance state vector, the interface conditions, Eq. (2.32), become

$$\mathcal{J}\left(\mathrm{i}\mu\alpha\widehat{v}+\mu\frac{\mathrm{d}\widehat{u}}{\mathrm{d}y}\right)=-\mathcal{J}\left(\mu U''^{I}\right)\widehat{f}, \tag{2.33}$$

$$\mathcal{J}\left[\mu\left(\frac{\mathrm{d}}{\mathrm{d}y}-1\right)\widehat{w}-\mu n\widehat{v}\right]=0, \tag{2.34}$$

$$\mathcal{J}\left(-\widehat{p}+\mathrm{i}\frac{2\mu}{Re}\frac{\mathrm{d}\widehat{v}}{\mathrm{d}y}\right)=\frac{1}{We}\left(1-n^2-\alpha^2\right)\widehat{f}. \tag{2.35}$$

Further, note that the radial stress component is valid at the interface location where $r=1$. Introduction of the boundary conditions, Eq. (2.24), and velocity interface conditions, Eq. (2.31), as well as the stress interface conditions, Eqs. (2.33)–(2.35), into Eq. (2.13) leads to a well-defined eigenvalue problem.

3. Optimal interface disturbances

3.1. *Optimization problem*

Exponential growth describes only one possible path for the amplification of disturbances. As noted, for instance, by Gustavsson (1991) and Trefethen *et al.* (1993) in the context of one-phase shear flows, the nonnormal nature of the linearized Navier-Stokes equations also permits the amplification of disturbances under exponentially stable conditions. Analysis of these types of non-exponentially growing solutions is commonly facilitated by solving an optimization problem in terms of a suitable measure such as the perturbation kinetic energy. In the following section, we seek linearly optimal conditions that maximize the resulting surface tension energy at the interface of the liquid jet. Following Hwang & Hack (2017) and Hack & Moin (2017), we construct a pseudo-propagator from the evolution of individual modes and analyze it by means of singular value decomposition.

The optimization target of our analysis is the magnitude of the interface distortion, which is measured by the interface energy norm

$$||q||_{IE} = B\widehat{f}^2. \tag{3.1}$$

Here, B is a parameter of the optimization procedure, which is set to 10 in this study. The introduction of a weight matrix F allows the transformation of the interface energy norm into a 2-norm so that $||\boldsymbol{q}||_{IE} \equiv ||\mathsf{F}\boldsymbol{q}||_2$. The norm, Eq. (3.1), partitions the state vector and as such describes a nontrivial semi-norm in which F is rank-deficient. Specifically, the velocity and pressure components of both the gas and the liquid phases are within the kernel of F.

The formulation of a well-posed optimization problem thus calls for the introduction of a full norm (Foures *et al.* 2012), which is chosen to be the total energy norm

$$\begin{aligned}||q||_E = \frac{1}{2}\Big[\eta \int_{r'=1}^{r'=L_g} \int_{\theta=0}^{\theta=2\pi} \left(|\widehat{u}_g|^2 + |\widehat{v}_g|^2 + |\widehat{w}_g|^2\right) r'\mathrm{d}r'\mathrm{d}\theta \\ + \int_{r'=0}^{r'=1} \int_{\theta=0}^{\theta=2\pi} \left(|\widehat{u}_l|^2 + |\widehat{v}_l|^2 + |\widehat{w}_l|^2\right) r'\mathrm{d}r'\mathrm{d}\theta + S\Big],\end{aligned} \tag{3.2}$$

where $S = |f|^2/We$ is the surface tension energy. Analogous to the interface energy norm, the energy norm can be converted to a 2-norm by means of the matrix F_N, with $||\boldsymbol{q}||_E \equiv ||\mathsf{F}_N\boldsymbol{q}||_2$. Since Eq. (3.2) takes into account all components of the state vector, the null space of F_N is empty.

The optimal initial and final conditions can be expressed as

$$\mathbf{q}_0 = \mathsf{Q}_0\boldsymbol{\kappa}, \qquad \mathbf{q}_1 = \mathsf{Q}_1\boldsymbol{\kappa}, \tag{3.3}$$

where the columns of Q_0 and Q_1 comprise the N least stable eigenfunctions at the initial and final times and $\boldsymbol{\kappa}$ assigns each of those modes a specific weight. The linear nature of the problem implies that $\boldsymbol{\kappa}$ is identical in both expressions. Since Q_0 has full column rank, we can directly compute its pseudoinverse Q_0^+, leading to

$$\mathsf{Q}_0^+\mathsf{q}_0 = \boldsymbol{\kappa}. \tag{3.4}$$

Substitution into Eq. (3.3) yields

$$\mathbf{q}_1 = \mathsf{Q}_1\mathsf{Q}_0^+\mathbf{q}_0 = \mathcal{L}_1\mathbf{q}_0, \tag{3.5}$$

where $\mathcal{L}_1$ is a pseudo-propagator that advances arbirary initial disturbances $\mathbf{q}_0$ within the column space of Q_0 from t_0 to t_1. The objective of finding the specific initial condition $\boldsymbol{q}_0$ that maximizes the magnitude of interface distortions at a given target time t_1 may thus be expressed as the functional

$$\begin{aligned}G(t) &= \max_{\boldsymbol{q}_0} \frac{||\boldsymbol{q}_1||_{IE}^2}{||\boldsymbol{q}_0||_E^2} = \max_{\boldsymbol{q}_0} \frac{||\mathcal{L}_1\boldsymbol{q}_0||_{IE}^2}{||\mathcal{L}_0\boldsymbol{q}_0||_E^2} = \max_{\boldsymbol{q}_0} \frac{||\mathsf{F}\mathcal{L}_1\boldsymbol{q}_0||_2^2}{||\mathsf{F}_N\mathcal{L}_0\boldsymbol{q}_0||_2^2} \\ &= \max_{\boldsymbol{q}_0} \frac{||\mathsf{F}\mathcal{L}_1(\mathsf{F}_N\mathcal{L}_0)^+\mathsf{F}_N\mathcal{L}_0\boldsymbol{q}_0||_2^2}{||\mathsf{F}_N\mathcal{L}_0\boldsymbol{q}_0||_2^2} = ||\mathsf{F}\mathcal{L}_1(\mathsf{F}_N\mathcal{L}_0)^+||_2^2.\end{aligned} \tag{3.6}$$

Note that the introduction of $\mathcal{L}_0 = \mathsf{Q}_0\mathsf{Q}_0^+$ into the denominator restricts $\mathbf{q}_0$ to the column space of Q_0. Further details on this formulation are provided in Hwang & Hack (2017).

3.2. *Initial value problem*

The solution of the optimization problem by means of singular value decomposition provides the right and left singular vectors, which correspond to the optimal initial disturbance and the final disturbances. To compute the velocity disturbances at intermediate times, the eigenvalue problem, Eq. (2.13), is recast into an ordinary differential equation in time as

$$\mathsf{M}\frac{\mathrm{d}\boldsymbol{q}}{\mathrm{d}t} = \mathsf{L}\boldsymbol{q}. \tag{3.7}$$

The solution of this initial value problem can be facilitated, for instance, using a Crank-Nicolson scheme, which yields

$$\mathsf{M}\frac{\boldsymbol{q}^{n+1} - \boldsymbol{q}^{n}}{\Delta t} = \mathsf{L}\frac{\boldsymbol{q}^{n+1} + \boldsymbol{q}^{n}}{2}. \tag{3.8}$$

4. Energy budget

Analysis of the budget of perturbation kinetic energy provides insight into the mechanism that drives the amplification of perturbations. The energy budget is derived by taking the dot product of the linearized governing equations, Eqs. (2.2)–(2.4), with the velocity perturbation vector. Integration of the result over a control volume and application of the continuity equation, Eq. (2.5), as well as the interface boundary condition Eq. (2.32), show the material derivative of the perturbation kinetic energy,

$$\dot{E}_{KE} \equiv \frac{1}{2}\int_0^\lambda \int_0^{2\pi} \int_0^1 \left(\partial_t + U_l \partial_z\right)\left(u_l^2 + v_l^2 + w_l^2\right) r \,\mathrm{d}r d\theta dz, \tag{4.1}$$

to be governed by the following terms

$$\dot{E}_{KE} = \int_0^{2\pi} \Bigg(\underbrace{\int_0^\lambda \left[\frac{1}{We} v_l \left(1 - \alpha^2 - n^2\right) f\right]_{r=1} \mathrm{d}z}_{\text{Surface tension}} + \underbrace{\int_0^1 \int_0^\lambda \left(-v_l u_l U'\right) r \,\mathrm{d}r \,\mathrm{d}z}_{\text{Reynolds stress}} +$$

$$\underbrace{\int_0^\lambda \left[-p_g v_l\right]_{r=1} \mathrm{d}z}_{\text{Gas pressure fluctuation}} + \underbrace{\int_0^1 \left[-p_l u_l\right]_{z=0}^{z=\lambda} r \,\mathrm{d}r}_{\text{Liquid pressure fluctuation}} + \underbrace{\int_0^\lambda \left[f u_l \left(m\frac{\mathrm{d}^2 U_g^I}{\mathrm{d}r^2} - \frac{\mathrm{d}^2 U_l^I}{\mathrm{d}r^2}\right)\right]_{r=1} \mathrm{d}z}_{\text{Shear from base flow distortion}} +$$

$$\frac{1}{Re}\Bigg\{ \underbrace{\int_0^\lambda \left[m u_l \left(\frac{\mathrm{d}v_g}{\mathrm{d}z} + \frac{\mathrm{d}u_g}{\mathrm{d}r}\right)\right]_{r=1} \mathrm{d}z + \int_0^1 \left[v_l \left(\frac{\mathrm{d}u_l}{\mathrm{d}r} + \frac{\mathrm{d}v_l}{\mathrm{d}z} + w_l \frac{\mathrm{d}w_l}{\mathrm{d}z}\right)\right]_{z=0}^{z=\lambda} r \,\mathrm{d}r}_{\text{Shear stress}} +$$

$$\underbrace{\int_0^\lambda \left[2 m v_l \frac{\mathrm{d}v_g}{\mathrm{d}r} + w_l \frac{\mathrm{d}w_l}{\mathrm{d}r}\right]_{r=1} \mathrm{d}z + \int_0^1 \left[2 u_l \frac{\mathrm{d}u_l}{\mathrm{d}z}\right]_{z=0}^{z=\lambda} r \,\mathrm{d}r}_{\text{Normal viscous stress}} +$$

$$\underbrace{-\int_0^1 \int_0^\lambda \left(2\left(\frac{\mathrm{d}v_l}{\mathrm{d}r}\right)^2 + 2\left(\frac{\mathrm{d}u_l}{\mathrm{d}z}\right)^2 + \left(\frac{\mathrm{d}u_l}{\mathrm{d}r} + \frac{\mathrm{d}v_l}{\mathrm{d}z}\right)^2 + \frac{1}{2}\left(\frac{1}{r}\frac{\mathrm{d}w}{\mathrm{d}\theta}\right)^2\right) r \,\mathrm{d}r \,\mathrm{d}z}_{\text{Viscous dissipation}} +$$

$$\underbrace{-\int_0^1 \int_0^\lambda \left(\frac{1}{2}\left(\frac{\mathrm{d}w}{\mathrm{d}z}\right)^2 + \frac{1}{2}\left(\frac{1}{r}\frac{\mathrm{d}u}{\mathrm{d}\theta} + \frac{\mathrm{d}w}{\mathrm{d}z}\right)^2 + \frac{1}{2}\left(\frac{\mathrm{d}w}{\mathrm{d}r}\right)^2 + \frac{1}{2}\left(\frac{1}{r}\frac{\mathrm{d}v}{\mathrm{d}\theta} + \frac{\mathrm{d}w}{\mathrm{d}r}\right)^2\right) r \,\mathrm{d}r \,\mathrm{d}z}_{\text{Viscous dissipation}} +$$

$$\underbrace{-\int_0^1\int_0^\lambda \left(2\left(\frac{v}{r}+\frac{1}{r}\frac{\mathrm{d}w}{\mathrm{d}\theta}\right)^2+\frac{1}{2}\left(\frac{w}{r}\right)^2+\frac{1}{2}\left(\frac{1}{r}\frac{\mathrm{d}v}{\mathrm{d}\theta}-\frac{w}{r}\right)^2+\left(\frac{1}{r}\frac{\mathrm{d}w}{\mathrm{d}\theta}\right)^2\right) r\,\mathrm{d}r\,\mathrm{d}z}_{\text{Viscous dissipation}}\Bigg\}\Bigg)\, d\theta. \tag{4.2}$$

5. Results

5.1. *Base flow*

In the following section, we apply the linear analysis to a laminar jet injected into stationary air. The four nondimensional parameters, Eq. (2.1), are $Re = 750$, $We = 40$, $m = 0.015$ and $\eta = 1$, respectively. The base flow is computed from numerical simulations using a simulation code by Cascade Technology based on a volume-of-fluid representation of the two phases. Figure 1(a, b) shows a front view and a side view of the grid, respectively. Three million hexahedral control volumes were used to discretize the domain. The radius of the computational domain at the inlet is $8R$ and increases to $10R$ in the streamwise dimension to account for the expected expansion of the jet. Grid elements are nonuniformly spaced in the radial dimension, with a clustering of points near the liquid-gas interface. The streamwise extent of the computational domain is $100R$, with refined elements placed near the nozzle exit, while coarse buffer regions are added in both the radial and the axial regions to minimize the effect of boundaries on the solution in the computational domain. At the exit of the nozzle, a fine grid spacing of size $\Delta = 0.03$ is used, whereas grid elements of size $\Delta = 0.5$ are used in the buffer region.

The base flow at a streamwise location $8R$ downstream from the nozzle exit is time averaged for 100 characteristic time units, T, defined as the ratio of the characteristic length and velocity, $T = R/U$. Figure 2 shows the base flow from the numerical simulation that used are in the linear stability analysis. Note that the interface is located at $r = 1$.

5.2. *Linear stability analysis*

The result of the linear stability analysis of the jet reveals the first four azimuthal wavenumbers, $n = 0$ to $n = 3$, to be unstable. Figure 3 shows the growth rate of the unstable cases, indicating exponential amplification for a range of streamwise wavenumbers. The highest growth rate of $\omega_i = 0.11$ is observed for the $n = 1$ case at $\alpha = 1.2$ (see, e.g., Hoyt & Taylor 1977; Chigier 1989). On the other hand, disturbances with azimuthal wavenumbers $n = 4$ to $n = 7$ show negative growth rates for the full range of streamwise wavenumbers considered. In order to find the most effective interface distortion for these cases, we consider the optimization problem introduced above.

Figure 4 presents the optimized interface energy ratio for combinations of $\alpha \in [0.0, 3.0]$ and $n \in \{4, 5, 6, 7\}$. Values larger than 1 indicate an amplification of surface tension energy at a certain target time compared to the initial state through a nonexponentially amplifying mechanism. To illustrate the behavior of the interface distortion in greater detail, we inspect the specific exponentially stable parameter combination $\alpha = 1.2$ and $n = 4$. The solution to the optimization problem in form of the initial optimal velocity disturbance and pressure disturbance is presented in Figure 5(a, b). This specific initial condition evolves during the target time interval $\Delta t = 1.7$ into the final state presented in Figure 5(c, d). During this interval, the magnitude of the interface distortion grows from $|f| = 1.84 \times 10^{-4}$ to $|f| = 1.505$. This appreciable growth of the interface disturbance by nearly five orders of magnitude suggests a possible pathway for the generation of interface distortions large enough to promote the eventual atomization of a jet even for

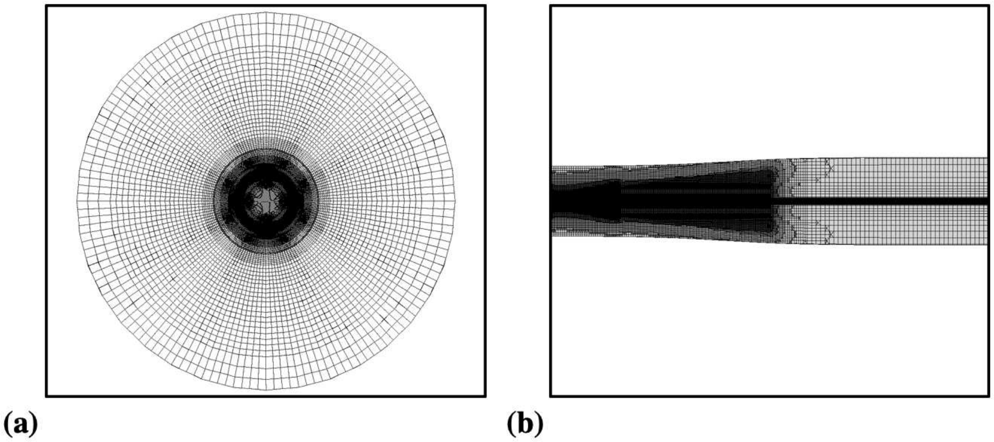

FIGURE 1. Grid used in the numerical simulation to compute the base flow. (a) Inlet front view and (b) side view of the grid.

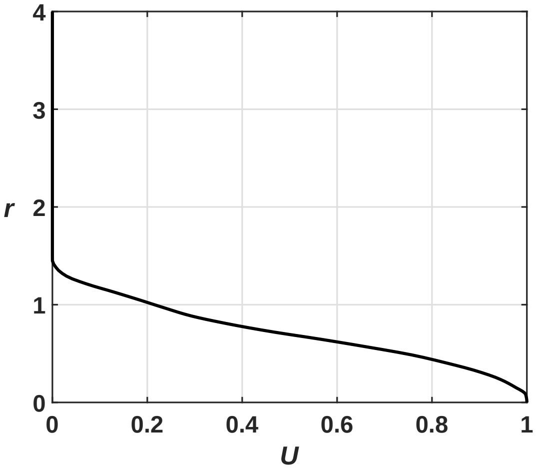

FIGURE 2. Base flow computed from the numerical simulation and used in the linear stability analysis.

exponentially stable flow configurations. The time evolution of the normalized interface energy norm and the magnitude of the interface disturbance for the current choice of parameters are respectively presented in Figures 6(a) and (b).

Insight into the underlying mechanisms of the growth of the interface energy is gained from an analysis of the budget of the perturbation kinetic energy. To limit the complexity of the results, we consider the three most dominant terms from the total budget, Eq. (4.2), which are the surface tension energy term, the Reynolds stress term and the gas pressure fluctuation term. Figure 7 shows the kinetic energy flux during the evolution of the initial condition identified in the solution of the optimization problem. The Reynolds stress term and the pressure-velocity-correlation term are positive and initially grow, whereas the surface tension term is negative and decreases, implying that the first two terms increase the total perturbation kinetic energy of the system. On the other hand, the

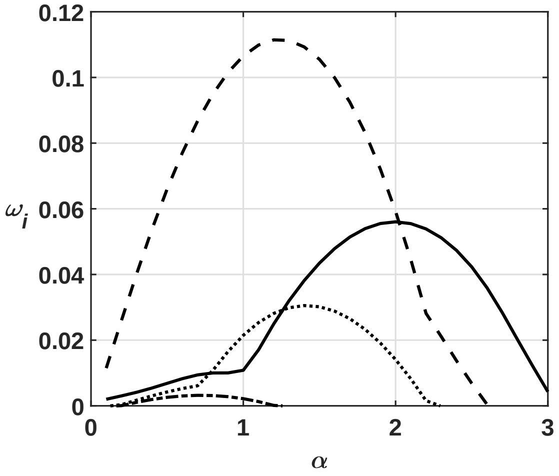

FIGURE 3. Growth rate for unstable cases. Solid line: $n = 0$; dashed line: $n = 1$; dotted line: $n = 2$; dash dotted line: $n = 3$.

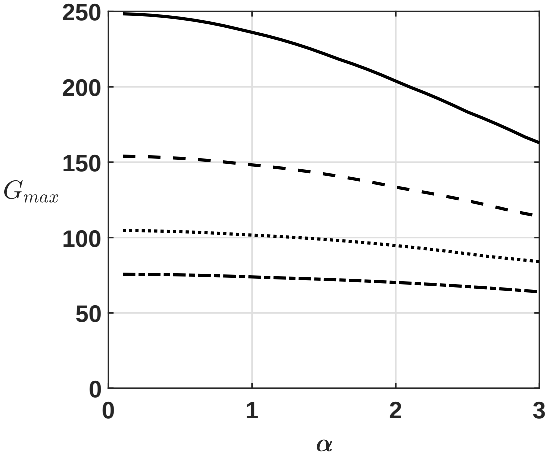

FIGURE 4. The maximum value of the ratio of the interface energy at a given streamwise wavenumber and azimuthal wavenumber. Solid line: $n = 4$; dashed line: $n = 5$; dotted line: $n = 6$; dash–dotted line: $n = 7$.

surface tension term drains the perturbation kinetic energy. The overall flow of energy is thus from the mean shear and the gas–phase pressure acting on the surface into surface tension energy, which is related to the magnitude of the interface distortion.

6. Conclusions

The amplification of interface distortions of jets, with particular focus on settings that are stable to exponential instabilities, was considered. The base flow was computed in a numerical simulation using a volume-of-fluid formulation. The stability of the flow was

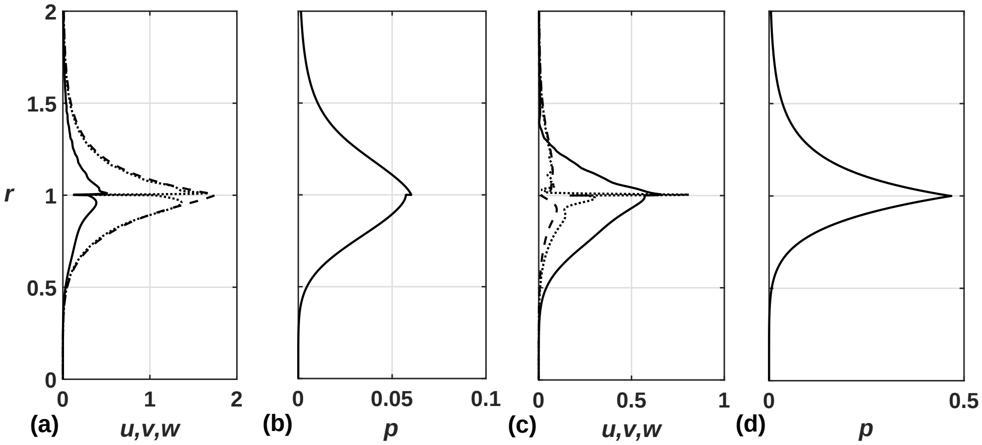

FIGURE 5. The initial optimal disturbance of (a) velocity disturbance and (b) pressure disturbance. The final optimal disturbance of (c) velocity disturbance and (d) pressure disturbance. For (a, c) solid line: streamwise velocity disturbance; dashed line: radial velocity disturbance; dotted line: azimuthal velocity disturbance.

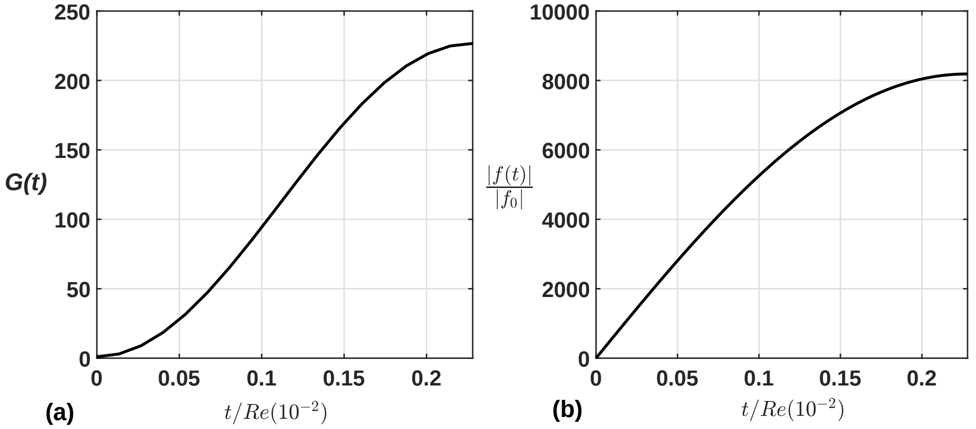

FIGURE 6. (a) The ratio of the interface energy norm at a target time to that at the initial time. (b) The ratio of the interface distortion to the initial interface distortion in time.

investigated using linear theory and an interface energy norm was introduced as a measure of the potential energy stored in the distortion of the jet interface. An optimization problem was formulated to identify the specific initial condition, which during a given time interval maximizes the energy of surface distortions. The energy budget for a three-dimensional nonaxisymmetric jet in a two-phase setting was derived.

Results for a representative test case demonstrated a possible pathway for the amplification of interface distortions in the absence of exponential instabilities. Analysis of the energy budget shows that during this process, energy is transferred from the mean flow to perturbations and ultimately to the potential energy of the interface. The optimal initial condition amplifies the magnitude of the interface by almost five orders of magnitude

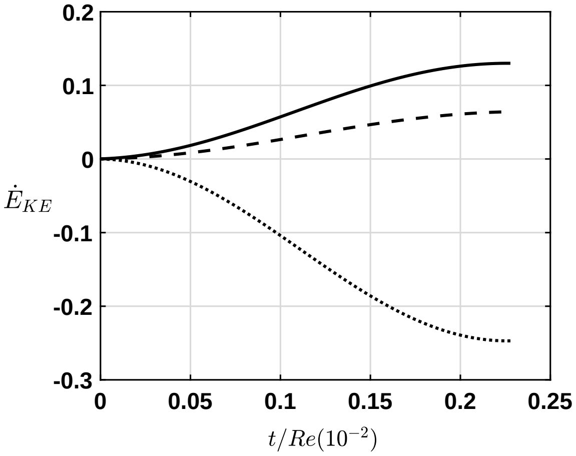

FIGURE 7. Kinetic energy flux from the initial optimal state to the final optimal state. Solid line: pressure–radial velocity correlation term; dashed line: Reynolds stress term; dotted line: surface tension energy term.

over a finite time interval. As such, optimal surface distortions may describe a pathway for advancing the primary atomization process of jets in exponentially stable settings.

Acknowledgments

This study was supported by the Office of Naval Research (ONR), Grant No. N00014-15-1-2726.

REFERENCES

BAGUE, A., FUSTER, D., POPINET, S., SCARDOVELLI, R. & ZALESKI, S. 2010 Instability growth rate of two-phase mixing layers from a linear eigenvalue problem and an initial-value problem. *Phys. Fluids* **22**, 092104.

BORONIN, S. A., HEALEY, J. J. & SAZHIN, S. S. 2013 Non–modal stability of round viscous jets. *J. Fluid Mech.* **716**, 96–119.

CHIGIER, N. 1989 Atomization of liquid jets from injection element in liquid rocket combustion chamber. *Second Quarterly Report to NASA*

FOURES, D. P. G., CAULFIELD, C. P & SCHMID, P. J. 2012 Variational framework for flow optimization using seminorm constraints. *Phys. Rev.* **86**, 026306.

GUSTAVSSON, L. H. 1991 Energy growth of three-dimensional disturbances in plane Poiseuille flow. *J. Fluid Mech.* **224**, 241–260.

HACK, M. J. P. & MOIN, P. 2017 Algebraic disturbance growth by interaction of Orr and lift-up mechanisms. *J. Fluid Mech.* **829**, 112–126.

HOYT, J. W. & TAYLOR, J. J. 1977 Waves on water jets. *J. Fluid Mech.* **83**, 119.

HU, H. H. & JOSEPH, D. D. 1989 Lubricated pipelining: stability of core–annular flow. Part 2. *J. Fluid Mech.* **205**, 359–396.

HWANG, H. & HACK, M. J. P. 2017 Optimal distrubances in two–phase mixing layers. *Annual Research Briefs*, Center for Turbulence Research, Stanford University, pp. 43-54.

Khorrami, M. R., Malik, M. R. & Ash, R. L. 1989 Application of spectral collocation techniques to the stability of swirling flows. *J. Fluid Mech.* **81**, 206–229.

Kim, D. & Moin, P. 2011 Numerical simulation of the breakup of a round liquid jet by a coaxial flow of gas with a subgrid Lagrangian breakup model. *Annual Research Briefs*, Center for Turbulence Research, Stanford University, pp. 15-30.

Lasheras, J. C. & Hopfinger, E. J. 2000 Liquid jet instability and atomization in a coaxial gas stream. *Annu. Rev. Fluid Mech.* **32**, 275–308.

Lin, S. P. & Chen, J. N. 1998 Role played by the interfacial shear in the instability mechanism of a viscous liquid jet surrounded by a viscous gas in a pipe. *J. Fluid Mech.* **376**, 37–51.

Lin, S. P. & Ibrahim, E. A. 1990 Instability of a viscous liquid jet surrounded by a viscous gas in a vertical pipe. *J. Fliud Mech.* **218**, 641–658.

Marmottant, P. & Villermaux, E. 2004 On spray formation. *J. Fluid Mech.* **498**, 73–111.

Morris, P. J. 1976 The spatial viscous instability of axisymmetric jets. *J. Fluid Mech.* **77**, 511–529.

Preziosi, L., Chen, K. & Joseph, D. D. 1989 Lubricated pipelining: stability of core–annular flow. *J. Fluid Mech.* **201**, 323–356.

Reddy, S. C. & Henningson, D. S. 1993 Energy growth in viscous channel flow. *J. Fluid Mech.* **252**, 209–238.

Schmid, P. J. & Henningson, D. S. 1994 Optimal energy density growth in Hagen–Poiseuille flow. *J. Fluid Mech.* **277**, 197–225.

Schmid, P. J. & Henningson, D. S. 2001 Stability and Transition in Shear Flows. *Springer–Verlag.*

South, M. J. & Hooper, A. P. 1999 Linear growth in two–fluid plane Poiseuille flow. *J. Fluid Mech.* **381**, 121–139.

Trefethen, L. N., Trefethen, A. E., Reddy, S. C. & Driscoll, T. A. 1993 Hydrodynamic stability without eigenvalues. *Science* **261**, 578–584.

Xie, L., Yang, L. & Ye, H. 2017 Instability of gas–surrounded Rayleigh viscous jets: weakly nonlinear analysis and numerical simulation. *Phys. Fluids* **29**, 074101.

Yecko, P., Zaleski, S. & Fullana, J. M. 2002 Viscous modes in two-phase mixing layers. *Phys. Fluids* **14**, 4115.